Open Access

Earth System
Science
Data

GCI30: a global dataset of 30 m cropping intensity using multisource remote sensing imagery

Miao Zhang[1], Bingfang Wu[1,2], Hongwei Zeng[1,2], Guojin He[1,2], Chong Liu[3], Shiqi Tao[4], Qi Zhang[5,6],
Mohsen Nabil[1,2,7], Fuyou Tian[1,2], José Bofana[1,2,8], Awetahegn Niguse Beyene[1,2,9],
Abdelrazek Elnashar[1,2,10], Nana Yan[1], Zhengdong Wang[1,2], and Yiliang Liu[11]

[1]State Key Laboratory of Remote Sensing Science, Aerospace Information Research Institute, Chinese
Academy of Sciences, Beijing 100101, PR China
[2]College of Resources and Environment, University of Chinese Academy of Sciences,
Beijing 100049, PR China
[3]School of Geospatial Engineering and Science, Sun Yat-Sen University, Guangzhou, 510275, PR China
[4]Graduate School of Geography, Clark University, Worcester, MA 01610, USA
[5]Department of Earth and Environment, Boston University, Boston, MA 02215, USA
[6]Frederick S. Pardee Center for the Study of Longer-Range Future, Frederick S. Pardee School of Global
Studies, Boston University, Boston, MA 02215, USA
[7]Division of Agriculture Applications, Soils, and Marine (AASMD), National Authority for Remote Sensing
and Space Sciences (NARSS), Cairo, New Nozha, Alf Maskan, 1564, Egypt
[8]Center for Agricultural and Sustainable Development Research (CIADS), Faculty of Agricultural Sciences,
Catholic University of Mozambique, Cuamba 3305, Mozambique
[9]Tigray Agricultural Research Institute, P.O. Box 492, Mekelle 251, Ethiopia
[10]Department of Natural Resources, Faculty of African Postgraduate Studies,
Cairo University, Giza 12613, Egypt
[11]National Remote Sensing Center of China, Beijing 100036, PR China

Correspondence: Bingfang Wu (wubf@aircas.ac.cn) and Chong Liu (liuc@mail.sysu.edu.cn)

Abstract. The global distribution of cropping intensity (CI) is essential to our understanding of agricultural land use management on Earth. Optical remote sensing has revolutionized our ability to map CI over large areas in a repeated and cost-efficient manner. Previous studies have mainly focused on investigating the spatiotemporal patterns of CI ranging from regions to the entire globe with the use of coarse-resolution data, which are inadequate for characterizing farming practices within heterogeneous landscapes. To fill this knowledge gap, in this study, we utilized multiple satellite data to develop a global, spatially continuous CI map dataset at 30 m resolution (GCI30). Accuracy assessments indicated that GCI30 exhibited high agreement with visually interpreted validation samples and in situ observations from the PhenoCam network. We carried out both statistical and spatial comparisons of GCI30 with six existing global CI estimates. Based on GCI30, we estimated that the global average annual CI during 2016–2018 was 1.05, which is close to the mean (1.09) and median (1.07) CI values of the existing six global CI estimates, although the spatial resolution and temporal coverage vary significantly among products. A spatial comparison with two satellite-based land surface phenology products further suggested that GCI30 was not only capable of capturing the overall pattern of global CI but also provided many spatial details. GCI30 indicated that single cropping was the primary agricultural system on Earth, accounting for 81.57 % (12.28×10^6 km^2) of the world's cropland extent. Multiple-cropping systems, on the other hand, were commonly observed in South America and Asia. We found large variations across countries and agroecological zones, reflecting the joint control of natural and anthropogenic drivers on regulating cropping practices. As the

first global-coverage, fine-resolution CI product, GCI30 is expected to fill the data gap for promoting sustainable agriculture by depicting worldwide diversity of agricultural land use intensity. The GCI30 dataset is available on Harvard Dataverse: https://doi.org/10.7910/DVN/86M4PO (Zhang et al., 2020).

1   Introduction

The interrelated targets of zero hunger, no poverty, and promoting sustainable agriculture have been collectively recognized as the core sustainable development goals (SDGs) by the United Nations (UN, 2015; Wu et al., 2017; Whitcraft et al., 2019; Hinz et al., 2020). However, 750 million people are currently exposed to severe food insecurity, and the COVID-19 pandemic may have added approximately 100 million people to the total undernourished population in 2020 (FAO et al., 2020). Projections have further demonstrated that from 2010 to 2050, the world's agricultural production must increase by 70 %–110 % to meet the demands caused by increasing populations and changing diets (Tilman et al., 2011). However, intensified agricultural activities have many ripple effects on terrestrial ecosystems, including forest degradation (Morton et al., 2006; Zeng et al., 2018), soil pollution (Lal, 2002; Jankowski et al., 2018), and changes in carbon and water flux seasonality (Gray et al., 2014; Hao et al., 2015), which in turn damage the welfare of human society. To meet the critical human needs for food security and environmental sustainability, it is of major scientific significance to better understand how existing agricultural land resources are utilized, both locally and globally.

Cropping intensity (CI), defined as the number of crop planting and harvesting cycle(s) within a full year (Gray et al., 2014; C. Liu et al., 2020), offers a measure of cropland utilization that has profound implications for closing food production gaps and agricultural intensification (Challinor et al., 2015; Ding et al., 2016; Wu et al., 2018; Waha et al., 2020). CI also plays an essential role in crop modelling that assesses grain yield (Becker and Johnson, 2001), soil quality (Sherrod et al., 2003), and the impacts of climate change (Pielke et al., 2007; Challinor et al., 2015). Given its importance, it is necessary to accurately estimate CI to improve the management of agricultural activities as well as their interactions with other physical components of the Earth system. Before the advent of remote sensing, information about CI could be estimated only based on limited agricultural census data, but these data are often outdated and variable in accuracy (L. Liu et al., 2020). Remote sensing has revolutionized our ability to estimate CI, especially at continental to global scales (L. Liu et al., 2020). The presence of crop growth and senescence phenology constitutes the most characteristic temporal feature of agricultural practices, and numerous attempts have been made to link high-temporal-frequency vegetation index time series to CI identification. A growing season peak detection-based algorithm was developed

and used to monitor the CI spatiotemporal change in China (Yan et al., 2014, 2019). A similar approach was adopted by Kotsuki and Tanaka (2015) to derive a global crop calendar dataset containing CI metrics. Despite their prominent contributions to cropland intensification assessments, most existing CI products have coarse spatial resolutions, giving rise to the common presence of mixed pixels that can lead to a decreased CI mapping accuracy. To alleviate this issue, in recent years, fine-resolution optical satellite sensors, such as Landsat and Sentinel-2, have been employed to extract CI information. For example, Jain et al. (2013) found that fine-resolution satellite imagery can more accurately depict the CI pattern in smallholder agriculture regions than coarse-resolution satellite data. Hao et al. (2019) also reported an improved performance of CI identification using harmonized Landsat Sentinel-2 (HLS) data.

It is becoming increasingly clear that a global, fine-resolution CI product is essential for monitoring the ongoing cropland intensification process on Earth. However, to the best of our knowledge, such a dataset has not yet been created, reflecting the necessity of a generalizable CI mapping framework that is representative of diverse climate zones and cropping systems. To overcome this challenge, we proposed a phenophase-based CI mapping framework in our pilot study (C. Liu et al., 2020) with the use of multiple satellite data and the Google Earth Engine (GEE) platform (Gorelick et al., 2017), offering both methodological and practical bases for operationalizing a global fine-resolution CI product. Taking advantage of the proposed framework, the primary goal of this research is to advance and develop a global, spatially continuous CI map at a 30 m resolution (GCI30). To achieve this goal, we regenerated the global cropland extent layer and modified the CI estimation algorithm on flooded rice paddies by considering the flooding and transplanting signals. We integrated the full archive of Landsat, Sentinel-2, and MODIS data from 2016 to 2018 for constructing seamless spectral time series in order to capture the full cropping cycles, which is the key for CI identification by segmenting growing and non-growing periods. The performance of GCI30 was examined with in situ data as well as with six existing global products containing CI metrics. With a much finer spatial resolution and global coverage, GCI30 is expected to contribute to our fundamental understanding of the dynamics of the Earth's terrestrial surface as well as the human role in land modification through agricultural activities.

2 Materials and methods

2.1 GCI30 input data

2.1.1 Cropland extent

The cropland definition adopted in this study is based on the concept presented by the Joint Experiment of Crop Assessment and Monitoring (JECAM) network, which uses a shared definition of the cropland that matches the Food and Agriculture Organization's (FAO) Land Cover Meta Language. The annual cropland (including area affected by crop failure) is defined as a piece of arable land that is sowed or planted at least once within a 12-month period (Waldner et al., 2016). One exception to the above-mentioned cropland definition is the fields used for sugarcane and cassava cultivation, which are included in the cropland class, although they have a longer vegetation cycle and are not annually planted and harvested. We integrated 10 existing land cover maps or cropland datasets to delimit the global cropland extent while masking out irrelevant non-cropland pixels for the period of 2016–2018 (Fig. 1). Readers can refer to Table S1 in the Supplement for detailed information on these land cover and cropland layer products as well as their classes used in the integration. Although variations in classification systems among different products exist, a subset of classes of those land cover and cropland layer products were selected to best fit into the cropland definition. Spatially, FROM-GLC was selected for Europe, Africa, New Zealand, the majority of Asia, and part of Latin America. GFSAD30 was selected for tropical Asian islands, including Indonesia, Malaysia, and the Philippines. In addition to these two global-coverage cropland extent products, several national or regional datasets, including ChinaCover, CDL, AAFC ACI, NLCD, MapBiomass, CLUM, SERVIR, and INTA, were used because they have been extensively validated by local experts and hence exhibited high accuracies of cropland mapping. Their spatial extents cover China, the contiguous US, Canada, Alaska, Brazil, Australia, the lower Mekong River basin (Myanmar, Thailand, Lao, Cambodia, and Vietnam), and part of Argentina, respectively.

2.1.2 Satellite images and vegetation indices

All available images of top-of-atmosphere (TOA) reflectance from Landsat 7 ETM+, Landsat 8 OLI, and Sentinel-2 MSI during 2016–2018 were used for global CI mapping via the GEE platform. Invalid observations, including clouds, cloud shadows, snow, and saturated values, were identified and masked by the function of the mask (Fmask) algorithm (Zhu and Woodcock, 2012; Qiu et al., 2019). To overcome the multi-sensor mismatch issue, we adopted an inter-calibration approach, which converted Sentinel-2 MSI and Landsat 8 OLI TOA reflectance data to the Landsat 7 ETM+ standard (Chastain et al., 2019). Then the calibrated images were used

to composite the 16 d TOA reflectance time series (labelled as origin).

Based on the harmonized TOA reflectance composite, the following vegetation indices including the normalized difference vegetation index (NDVI), enhanced vegetation index (EVI), and land surface water index (LSWI) were calculated:

$$NDVI = \frac{\rho_{NIR} - \rho_{RED}}{\rho_{NIR} + \rho_{RED}} \tag{1}$$

$$EVI = 2.5 \times \frac{\rho_{NIR} - \rho_{RED}}{\rho_{NIR} + 6 \times \rho_{RED} - 7.5 \times \rho_{BLUE} + 1} \tag{2}$$

$$LSWI = \frac{\rho_{NIR} - \rho_{SWIR}}{\rho_{NIR} + \rho_{SWIR}}, \tag{3}$$

where ρ_{BLUE}, ρ_{RED}, ρ_{NIR}, and ρ_{SWIR} are the TOA reflectance values of the blue, red, near-infrared, and shortwave-infrared bands, respectively. We also used the MODIS Vegetation Index (MOD13Q1) Version 6 products (NDVI and EVI) and LSWI derived from MODIS Surface Reflectance (MOD09A1) Version 6 products to fill data gaps caused by the vacancy of Landsat and Sentinel-2 observations that were masked out by the Fmask algorithm. In particular, the coarse MODIS datasets were resized to 30 m using the bicubic interpolation method. Then an empirical linear function was built for each pixel to bridge the data records of MODIS and Landsat and Sentinel-2, and missing data gaps were filled with the resampled, transformed MODIS data (labelled as MODIS modelled). If there is no valid data from either Landsat and Sentinel-2 or MODIS, temporally adjacent (within 48 d) cloud-free Landsat and Sentinel-2 observations were used to determine the filling value (labelled as interpolated). After gap-filling, a weighted Whittaker smoother (Eilers, 2003; Kong et al., 2019; Zhang et al., 2019) was further adopted to smooth the gap-filled time series data. We assigned different weights (1, 0.5, 0.2) to Landsat and Sentinel-2 original observations, MODIS-modelled values, and interpolation values, respectively. Finally, a dataset of smoothed, seamless time series of vegetation indices was generated at a spatial resolution of 30 m with a temporal interval of 16 d.

2.2 Reference samples

The validation of the global CI product requires carefully constructed reference samples (Kontgis et al., 2015; Li et al., 2014; C. Liu et al., 2020). In this study, we constructed two independent reference datasets (termed RDsat and RDsite hereafter) (Fig. S1) to evaluate the GCI30 performance because currently no other product is capable of offering comprehensive CI mapping assessment at the global scale. The first dataset, RDsat, was generated based on a visual interpretation of satellite time series via the Geo-Wiki platform (Fritz et al., 2012). Based on the global segmentation of agroecological zones (termed AEZs here after) (Gommes et al., 2016, 2017) (Table S2), we applied a stratified sampling approach to ensure that RDsat was geographically representative across the globe. We divided all 65 AEZs into four
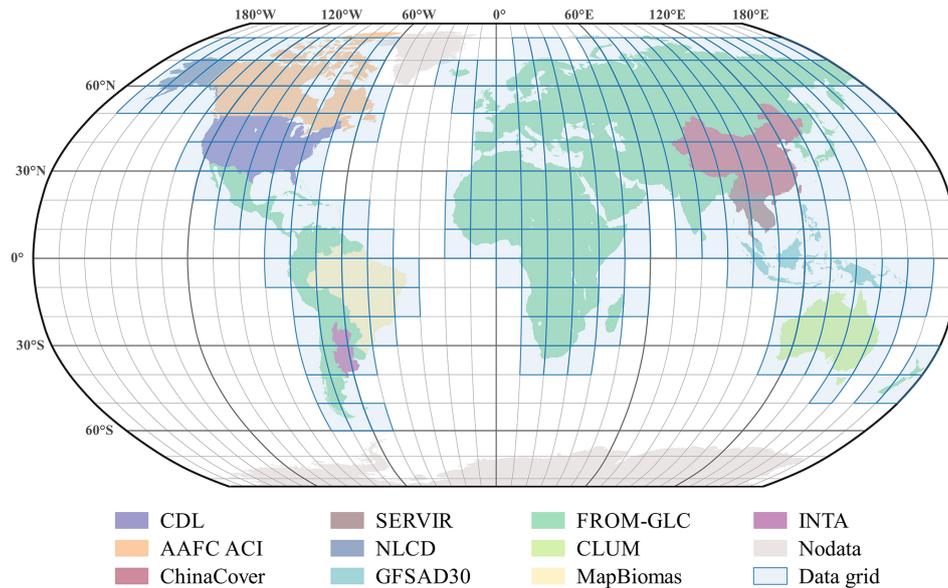
Figure 1. Spatial distribution of the land cover and cropland layer products used for the global 30 m cropland extent generation.

categories based on their cropland proportions: VL (cropland proportion < 4 %), L (4 % ≤ cropland proportion < 15 %), M (15 % ≤ cropland proportion < 40 %), and H (cropland proportion ≥ 40 %). For each category, 1000 plots (each equivalent to a 30 m Landsat pixel size) were randomly collected only within the cropland extent, and their phenological cycles during the period of 2016–2018 were visually counted. We have seven remote sensing experts (listed as co-authors) who checked all collected plots, and only well-interpreted plots with a high level of confidence were kept, leading to 3744 sample records. The second dataset, RDsite, was derived from the PhenoCam dataset (Richardson et al., 2018a, b; Seyednasrollah et al., 2019), which has been widely used as a robust in situ reference for remotely sensed phenology metric validation. Globally, there are 115 PhenoCam sites on cropland, and a total of 40 sites were collected after removing those with data records of less than 1 year (Table S3). For each selected site, we used the green chromatic coordinate (GCC) index (Richardson et al., 2018b) and in situ phenology camera image time series for cropping cycle number identification. It should be noted that not all the selected PhenoCam sites precisely covered a period matching 2016–2018. For instance, the site with the ID "usof6" in Table S3 provided measurements from May 2018 to September 2020, which was out of the study period used for our GCI30 product. However, to make full use of these measurements, we implemented our approach of CI identification by aligning the study period with the period containing the measurements at each of these sites. Thus, some CI identification covered longer periods than the 3-year length (2016–2018).

2.3 Global cropping intensity mapping method

2.3.1 CI mapping on non-flooded croplands

We applied the framework designed by C. Liu et al. (2020) for mapping global CI at the 30 m spatial resolution, using the phenophase-based approach for the non-flooded cropland and improving the algorithm to consider flooded rice paddy (Sect. 2.3.2). Targeting non-flooded cropland pixels, the methodology can be divided into two main steps, including (i) the identification of sub-period for a complete phenological phase of cropland within each cropland pixel and (ii) the derivation of cropping cycles for CI mapping.

With the smoothed, seamless NDVI time series, we identified a complete phenological cycle of crop via detecting the transitioning points that characterize the phenophase. Within the entire study period, 2016–2018, the transitioning points were located as 50 % of the NDVI amplitude (i.e. difference between the minimum and maximum values of observations) and labelled either greening-up points or greening-down points (Bolton et al., 2020). A point at the position where the slope of the time series function is positive is a greening-up point, while a point at the negatively changing time series is a greening-down point. A pair of points of these two types can separate NDVI time series into one staggered segment consisting of a growing sub-period and a non-growing sub-period.

Based on the segmented time series, we determined the potential number of complete phenophase cycles (N_{pc}) by taking the minimum value of the total numbers of transitioning points between the two types (greening-up and greening-down, labelled N_{up} and N_{down}, respectively) within the study period, formulated as

Earth Syst. Sci. Data, 13, 4799–4817, 2021

https://doi.org/10.5194/essd-13-4799-2021

$$N_{pc} = \min \left\{ N_{up}, N_{down} \right\}. \tag{4}$$

False cycles may exist due to the outliers of NDVI observations, with falsely detected cycles characterized by unrealistically short sub-periods pertaining to crop phenology (Yan et al., 2019). In other words, it is practically impossible for crop to be grown and harvested within a rather short time. In this case, we set a lower limit of the growing–harvesting cycle length to 48 d for removing the false cycles, noted as N_{fc}. By adjusting these falsely detected cycles and considering the 3-year study period (2016–2018), we calculated the annual cropping intensity (CI) for a non-flooded cropland pixel as

$$CI = \frac{N_{pc} - N_{fc}}{3}. \tag{5}$$

It should be noted that using the binary phenophase profile itself is not effective enough for identifying the continuous-cropping type, which is defined as cropping systems having short growing period (CI > 3 for this study) or exhibiting a lower degree of seasonality (e.g. tea plantation). Therefore, for each cropland pixel, we calculated the coefficient of variation (the ratio of the standard deviation to the mean, termed CV hereafter) of the NDVI time series and adopted a threshold method to determine whether the pixel belonged to the continuous-cropping type (low CV value). Specifically, within each AEZ, half of the RDsat samples labelled continuous cropping (if they existed) were adopted to obtain the CV threshold. This method generated an independent continuous-cropping type layer, which was integrated with the initially derived CI result.

2.3.2 CI mapping on flooded rice paddies

Flooded rice paddy, which accounts for more than 12 % of the global cropland area and feeds approximately half of the population (FAOSTAT, 2019; Ding et al., 2020), bears special mention in our study because it supports the only staple grains that need to be transplanted (Dong and Xiao, 2016), resulting in a relatively short non-growing period that may be mistakenly missed when using the above-mentioned approach. This issue becomes more prominent in areas with high cloud cover (e.g. Monsoon Asia). Therefore, we modified our approach in flooded rice paddy areas by considering the influence of the "flooding and transplanting signal" on the created phenophase profile (Fig. 2). Similar to the approach for non-flooded croplands, the NDVI time series trajectory was used to generate an initial phenophase profile (Fig. 2a). Then, within each identified growing season, the flooding and transplanting signals were detected and recognized based on the criteria LSWI > EVI or LSWI > NDVI (Fig. 2b), indicating that the water signal dominates the pixel spectral performance (Xiao et al., 2005; Dong et al., 2015, 2016). We regard the "flooding and transplanting" period as

a non-growing phenophase. Thus, the initial phenophase profile can be divided into two segments accordingly (Fig. 2c), reflecting the reality of double-season rice planting cycles. Finally, the CI information was determined by enumerating the transition points between different cropping cycles. Due to data limitations, this specific CI identification approach was applied only in southern China (AEZs C33, C37, C40, C41, and C42) and the lower Mekong River basin, where the paddy rice type was included in the land cover type scheme (derived from ChinaCover and SERVIR, respectively).

2.4 Accuracy assessment

Based on the RDsat and RDsite datasets, the accuracy assessment of GCI30 was conducted in two ways. In the first validation method, we directly evaluated the difference between the reference and estimated results. Here, the total number of cropping cycles (termed TNCC hereafter) rather than the actual CI value was used to avoid decimals. Four complementary indicators – systematic error (SE), mean absolute error (MAE), root mean square error (RMSE), and coefficient of determination (R^2) – were calculated as follows:

$$SE = \frac{1}{N} \sum_{i=1}^{N} \left(\hat{f}_i - f_i \right) \tag{6}$$

$$MAE = \frac{1}{N} \sum_{i=1}^{N} \left| \hat{f}_i - f_i \right| \tag{7}$$

$$RMSE = \sqrt{\frac{1}{N} \sum_{i=1}^{N} \left(\hat{f}_i - f_i \right)^2} \tag{8}$$

$$R^2 = 1 - \frac{\sum_{i=1}^{N} \left(\hat{f}_i - f_i \right)^2}{\sum_{i=1}^{N} \left(\hat{f}_i - \overline{f} \right)^2}, \tag{9}$$

where $\hat{f}_i$ and f_i are the estimated and reference cropping cycle number(s) for sample pixel i, respectively. N represents the number of samples, and $\overline{f}$ is the mean cropping cycle number value of all samples. In addition to directly quantifying the mapping errors, we further reclassified the GCI30 result into four categories: single cropping ($0 < CI \leq 1$), double cropping ($1 < CI \leq 2$), triple cropping ($2 < CI \leq 3$), and continuous cropping. We obtained the confusion matrix and calculated quantitative metrics, including overall accuracy (OA), kappa coefficient, producer accuracy (PA), and user accuracy (UA). Due to the limited sample sizes of RDsite, the classification-based accuracy assessment was conducted only for RDsat.

A systematic uncertainty analysis was further applied by interpolating the estimation biases from RDsat samples to a spatial distribution map (H. Liu et al., 2020). First, the linear normalization was conducted to transform the estimation bias range of RDsat samples to [0, 1]. Then the uncertainty
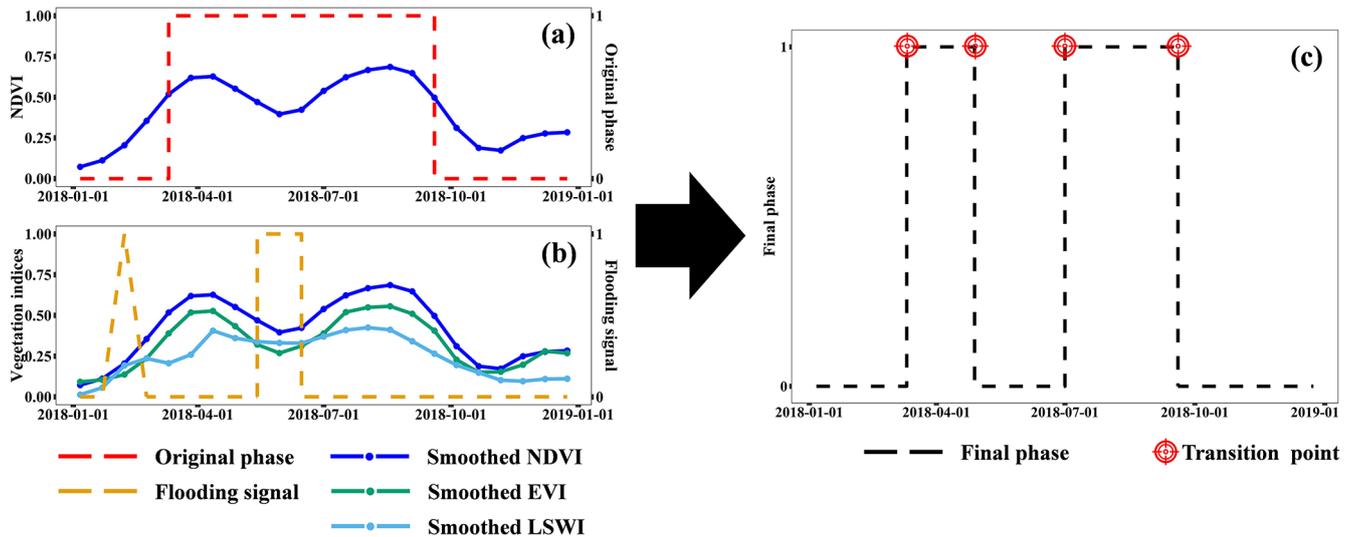
Figure 2. Illustration of the specific CI identification for a flooded rice paddy pixel.

map of GCI30 was created based on the Kriging interpolation method (Oliver and Webster, 1990). We used the ArcMap software of version 10.1 to implement the Kriging interpolation in this study, with the spatial search radius parameter set as the 12 nearest sample units. As a result, the values of generated uncertainty map range from 0 to 1. A smaller value indicates higher estimation reliability, while a higher value suggests a greater level of overestimation or underestimation of cropping cycle(s).

2.5 Comparison with other global products

Comparison of GCI30 with other global products or studies was conducted statistically and spatially (if available) at multiple levels. At the global level, we compared and evaluated the statistical differences between GCI30 and six existing statistics-based or satellite-based products (Table 1), including NASA's Vegetation Index and Phenology V004 (VIP4) dataset (Didan and Barreto, 2016), MODIS Land Cover Dynamics (MCD12Q2) Version 6 (Gray et al., 2019), SAtellite-derived CRop calendar for Agricultural simulations (SACRA) (Kotsuki and Tanaka, 2015), harvest frequency by Ray and Foley (2013) (R&F), actual cropping intensity (ACI) (Wu et al., 2018), and cropland use intensity (CUI) (Siebert et al., 2010). Among these products, four of them (MCD12Q2, VIP4, SACRA, and R&F) were further employed for national-level comparison. It should be noted that comparisons were only conducted for countries where both GCI30 and reference products are available. Finally, MCD12Q2 and VIP4 were used for pixel-by-pixel comparison against GCI30 due to their relatively fine spatial resolutions. To minimize uncertainty caused by temporal disagreement, we selected only the 2014 VIP4 and the 2016–2018 averaged MCD12Q2 data, within which the "Number of Seasons" layer of VIP4 and the "NumCycles" layer

of MCD12Q2 were extracted for intercomparison. We upscaled GCI30 to 0.05° and 500 m using the majority algorithm to match the spatial resolution of VIP4 and MCD12Q2, respectively. The same reclassification procedure described in Sect. 2.4 transformed the actual CI value of GCI30 and MCD12Q2 to match the VIP4 dataset's integer value range (0, 1, 2, 3), except for the continuous cropping and non-cropland pixels that were excluded from our comparison. We generated the difference maps among GCI30, VIP4, and MCD12Q2 to understand the overall overestimation or underestimation of our mapped CI results across continents.

3 Results and discussion

3.1 Reliability of GCI30

We examined GCI30 performance by generating a scatter plot of estimated and reference TNCC derived from RDsat and RDsite, respectively (Fig. 3). In general, GCI30 could provide reliable estimation results across different agro-environmental and management conditions, with relatively small MAE and RMSE values (equal to or less than 0.4 and 0.92, respectively) using the two reference datasets. Referring to R^2, GCI30 captured over 91 % of the variation in RDsite-derived TNCC and over 56 % of the variation in RDsat-derived TNCC. The discrepancies between RDsat-derived metrics and RDsite-derived metrics were mainly attributed to the differences in sample size and crop planting diversity. Specifically, the network of PhenoCam spots is spatially sparse, and most cropland sites are distributed in the United States featuring single-cropping systems (Fig. S1). There were slight systematic underestimations (negative SE) for GCI30, with the larger bias level occurring for RDsite. This result is consistent with C. Liu et al. (2020), indicating an overall conservative CI estimation by GCI30. In addition,

Earth Syst. Sci. Data, 13, 4799–4817, 2021

https://doi.org/10.5194/essd-13-4799-2021

Table 1. Existing cropping intensity products or studies used for intercomparison.

Existing products and studies	Algorithm	Input data	Temporal range used	Spatial resolution	Way of comparison
MCD12Q2	Phenometrics-based method	Time series MODIS EVI2	2016–2018	500 m	(1) Global level, (2) national level, (3) pixel level
VIP4	Half-maximum VI approach	Time series NDVI and EVI2 derived from both AVHRR and MODIS	2014	0.05°	(1) Global level, (2) national level, (3) pixel level
SACRA	Peak-counting considering crop calendar	Time series of SPOT-VEGETATION NDVI	2004–2006	5′	(1) Global level, (2) national level
R&F	The ratio of harvested cropland to total cropland	FAO statistics	2000–2011	National level	(1) Global level, (2) national level
ACI	Peak-counting	Time series GIMMS NDVI3g	2009–2011	8 km	(1) Global level
CUI	The ratio of harvested crop areas to total cropland area by excluding fallow land	MIRCA crop areas	2000	5′	(1) Global level

we found that larger estimation errors were commonly observed in samples with more cropping cycles. This tendency was not surprising because of the accumulated errors from every aspect of information extracted from remote sensing (Defourny et al., 2019), including data acquisition, time series modelling of vegetation indices, and phenological cycle identification. Therefore, we may expect that GCI30 faces larger challenges in terms of analysing multiple cropping systems.

Figure 4 further displays the spatial pattern of RDsat-based TNCC estimation bias across the globe. From 2016 to 2018, 79.8 % of the points exhibited unbiased predictions. Among the pixels with disagreement (i.e. non-zero bias), the majority were associated with one or two cropping cycle difference(s). Overall, there were more underestimation points (12.2 %) than overestimation points (8.0 %). Spatially, negative biases were mainly distributed in high-CI regions, including the Pampas (AEZ C26), central-eastern Brazil (AEZ C23), the Gulf of Guinea (AEZ C03), East African Highlands (AEZ C02), south of Himalaya (AEZ C44), and the Huanghuai-hai Plain (AEZ C34), altogether forming a northward "underestimation belt" along the longitudinal gradient. The negative errors could possibly be due to the complexity of some special cropping systems that cannot be fully accounted for by our CI mapping method. For example, inter-cropping or mixed cropping may lead to shallow troughs in NDVI time series, which makes the 50 % NDVI amplitude rule less reliable (C. Liu et al., 2020). Given the conservative CI estimation algorithm, it was somewhat unexpected to observe overestimation errors primarily concentrated in western Europe

(AEZ C60) and Ukraine to the Ural Mountains (AEZ C55), where the single-cropping practice dominates due to limited hydrothermal conditions (Wu et al., 2018). These positive biases could be attributed to the fallow strategy adopted in some Europe countries (Estel et al., 2016). During a fallow cycle, there may exist weeds which are falsely identified as one solid cropping cycle. In summary, the global bias distribution highlights the complex suite of biotic and abiotic processes that can obscure the effectiveness of the phenophase-based CI mapping framework.

Following the reclassification procedure illustrated in Sect. 2.4, we derived the corresponding confusion matrix of GCI30 using RDsat samples, with the quantitative accuracy metrics shown in Table 2. We found that GCI30 had reasonable classification performances, with OA and kappa coefficients greater than 92 % and 0.72, respectively. Regarding the classes of CI, single-cropping systems were associated with more robust classification results than were multiple-cropping systems. Comparatively, the single-cropping class was more subject to commission errors than omission errors (PA > UA), while the opposite tendency (PA < UA) was observed for the double- and triple-cropping classes. Continuous cropping is a fundamentally different agricultural land use management type from others. Here, we found that the continuous-cropping class of GCI30 had a higher PA (93.1 %) than UA (77.0 %). A possible explanation for this result is likely attributed to the threshold-based method for continuous-cropping identification. Some noncontinuous-cropping systems may also exhibit low CV values, leading to a relatively high commission error level.
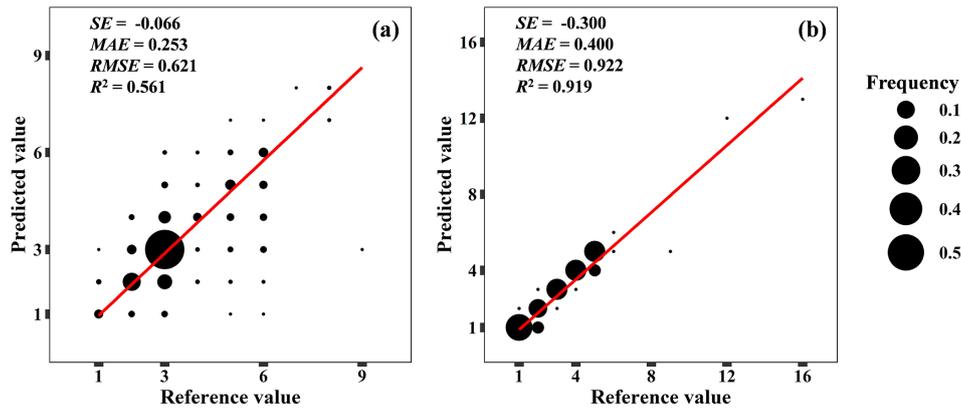
Figure 3. GCI30 accuracy assessment based on RDsat **(a)** and RDsite **(b)**. The red line represents the linear fitting line with the intercept forced to 0. The frequency of a specific reference–prediction value pair is proportional to its point size. Samples identified as continuous-cropping types were excluded.
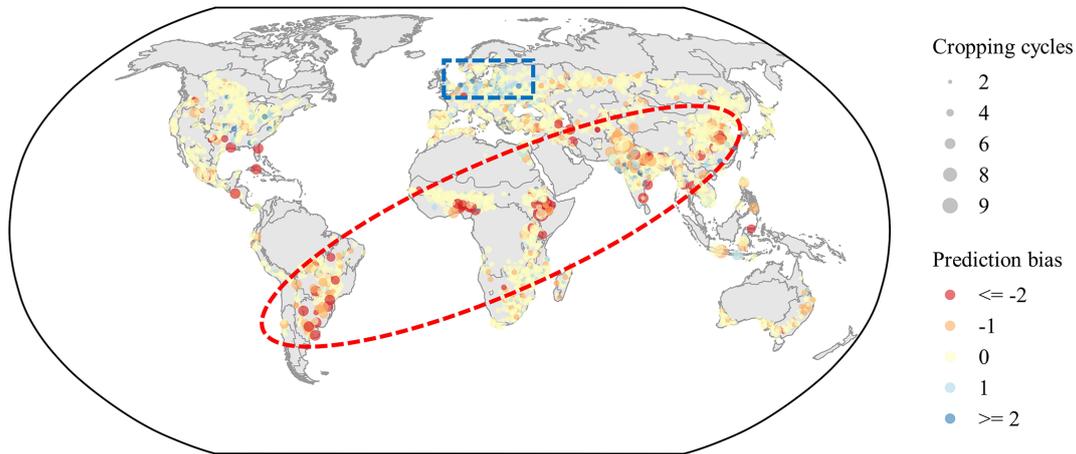

Figure 4. Spatial distribution of RDsat-based TNCC bias. The actual TNCC is proportional to its point size, and the prediction biases are identified by different point colours. Sample points identified as the continuous-cropping type were excluded. The blue rectangle indicates overestimations, and the red ellipsis region represents the northward "underestimation belt" along the longitudinal gradient.

Notably, although a stratified sampling strategy was conducted for creating RDsat, its sample size was still unbalanced among the different CI classes. The single-cropping class alone occupied 88.9 % of the total number of samples. Therefore, future efforts of GCI30 validation need to emphasize the inclusion of more samples with multiple-cropping systems.

A spatial distribution map of the GCI30 uncertainty was generated based on the RDsat. As shown in Fig. 5, most cropland areas display blue tones, indicating their low uncertainties and high estimation reliabilities of the GCI30. Spatially, relatively lower uncertainty levels were observed in Canada, the northern Great Plains in the United States, Russia, northern China, and southern Africa, where single cropping dominates. Meanwhile, there are still some areas of cropland with higher uncertainty as illustrated in orange and
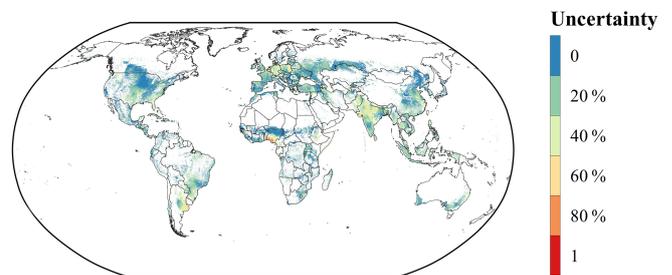

Figure 5. Global uncertainty map of GCI30 during 2016–2018, where regions in red represent higher uncertainty, and those in blue represent lower uncertainty.

red tones, mostly distributed in the Pampas, southern Nigeria, and central and northern India.

Table 2. Confusion matrices of GCI30.

	CI class type	Single	Double	Triple	Continuous	UA (%)
Reference	Single	3059	186			94.3
	Double	52	346	2	3	85.9
	Triple	1		6	2	66.7
	Continuous	9	9	2	67	77.0
	PA (%)	98.0	64.0	60.0	93.1	
	OA (%)		92.9			
	Kappa		0.728			

3.2 Spatial pattern of GCI30

GCI30 provides the first spatially continuous map of global CI at a 30 m resolution (Fig. 6). Based on this map, a heterogeneous pattern in CI compositions across continents was found, which are subject to varying anthropogenic and climate conditions. Overall, as expected, single cropping was the primary agricultural system on Earth, accounting for 81.57 % (12.28×10^6 km^2) of the world's cropland extent. Double cropping, on the other hand, was typically implemented in Asia, South America, and the Nile River basin of Africa, together occupying 17.42 % (2.62×10^6 km^2) of global croplands. Comparatively, the proportions of triple and continuous cropping were quite small, with their distributions mainly limited to Southeast Asia. According to the area statistics at 5° intervals, we found that the area of single cropping reached 54 % or higher in all latitude and longitude zones. The double-cropping distribution along latitude peaked in intervals ranging from 20 to 40° N, which encompassed China and India, the two most populous countries in the world. Along longitude, double cropping was mainly concentrated in three zones: 55 to 60° W, 75 to 90° E, and 100 to 125° E. These regions are commonly characterized by warm and humid climates, except for the Nile River basin, in which irrigation has been commonly used to support intensive farming practices (Zohaib and Choi, 2020). Over 75 % of triple- and continuous-cropping areas are located within tropical zones (5° S to 5° N). The tropical rainforest climate of these regions ensures sufficient water and heat supplies for crop growth throughout the year (Köppen et al., 2011).

Figure 7 displays the GCI30-based TNCC statistics at the continent level. We combined Australia and Oceania (New Zealand, Melanesia, Micronesia, and Polynesia) due to the rarity of cropland on these two continents. Globally, South America exhibited the most intensified cropping level, followed by Asia and Europe. Specifically, the average TNCC values were 3.67, 3.38, and 3.07 for South America, Asia, and Europe, respectively. South America and Asia also possessed the largest standard deviations of TNCC, indicating the inherent diversity of agricultural activities within these two continents as weather conditions directly affect cropping practices (Iizumi and Ramankutty, 2015). For exam-

ple, in Asia, triple- and continuous-cropping systems were distributed in Southeast Asia, including Indonesia, Malaysia, southern Thailand, and the Mekong River Delta in Vietnam. Double cropping was concentrated in the North China Plain, Ganga River basin and southern China, while the rest of Asia was dominated by a single-cropping pattern, covering central Asia, northeastern Asia, and southern India. Following these continents, moderate TNCC was found in North America (2.93 ± 0.54) and Africa (2.78 ± 0.71). Among all continents, the lowest TNCC occurred in Australia and Oceania (2.31 ± 0.77), where arid and semiarid climate types are dominant (Köppen et al., 2011; Beck et al., 2018).

At the global scale, the average CI pattern was heterogeneous across countries and AEZs (Fig. 8, left panel). Countries with the highest average CI levels were commonly detected in Asia (Bangladesh, Vietnam, Philippines, Sri Lanka) and Latin America (Guyana, Paraguay, Suriname, Haiti, and Dominican Republic). Together with Egypt, these top 10 countries exhibited TNCC values greater than 4.1 during 2016–2018. In contrast, low to moderate CI levels were typically found in high-latitude countries, such as Canada, Russia, and Mongolia. In addition to the latitude gradient, we found that the diversity of cropland management played a critical role in shaping the CI pattern. For example, some high-latitude European countries (Germany, Poland, Belarus, etc.) showed relatively high CI levels due primarily to their advanced cropland management practices (Guo, 2021). Rainfed agricultural practices lead to fewer cropping cycles in the Middle East and North African countries, except for Egypt, where most croplands are irrigated (Wu et al., 2018). Taking climate conditions into account, the heterogeneity of global CI becomes even more prominent among different AEZs. Arid regions, which cover vast areas in Africa, Australia, and Central Asia, are associated with fewer cropping cycles due to a lack of water for irrigation (Chiew et al., 2011; Guo et al., 2018) and less developed agricultural infrastructures (Mason-D'Croz et al., 2019). In contrast, intensive farming is widely distributed in humid and low-latitude areas such as South China and the Mekong Delta. Among all 65 AEZs, the Huanghuaihai Plain in China had the highest CI, followed by the Amazon rainforest region of South America and Taiwan
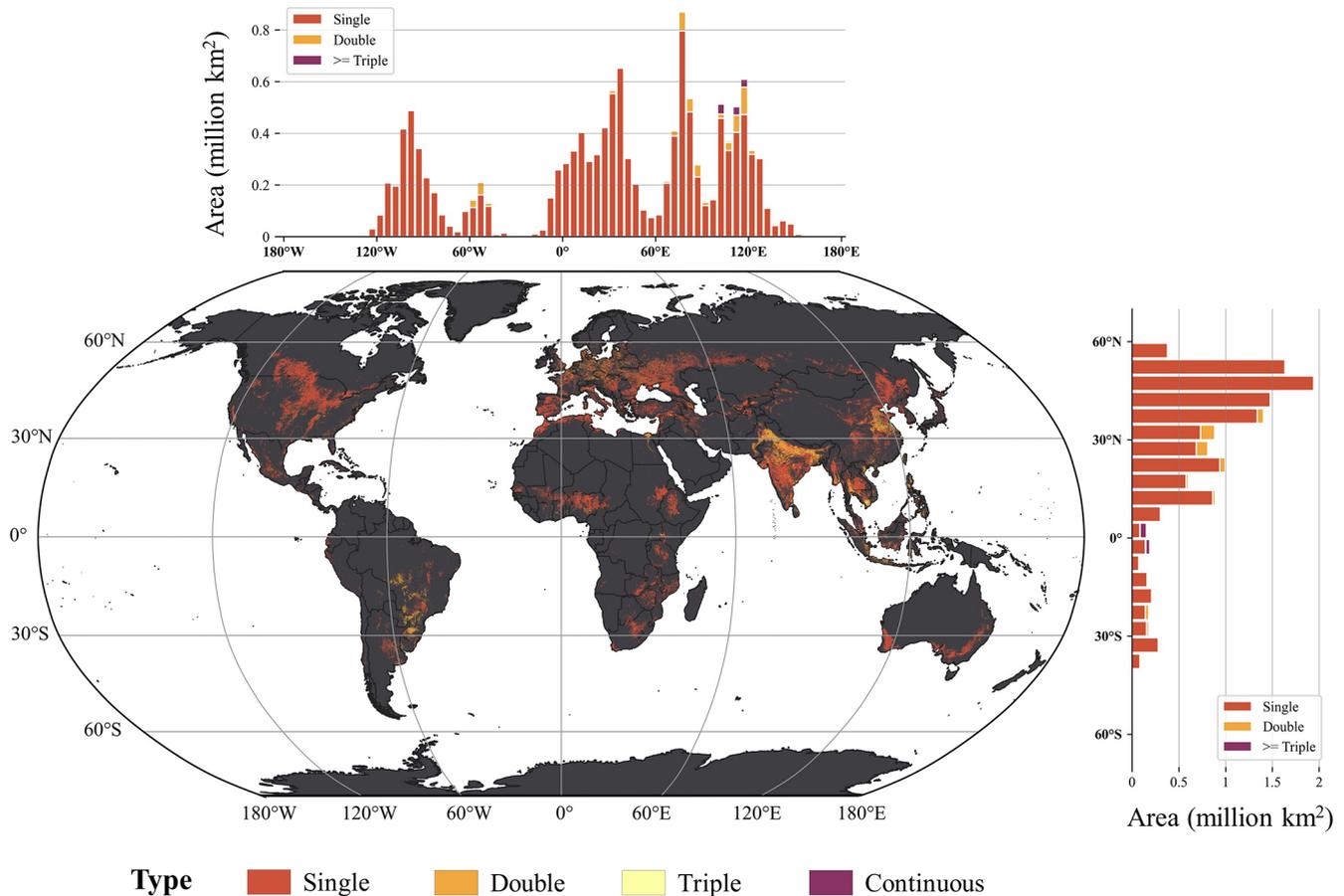
Figure 6. Geographical distribution of global CI types during 2016 to 2018 identified by GCI30. The area statistics along latitude and longitude are derived with an interval of $5°$. The area unit is 1×10^6 km^2.
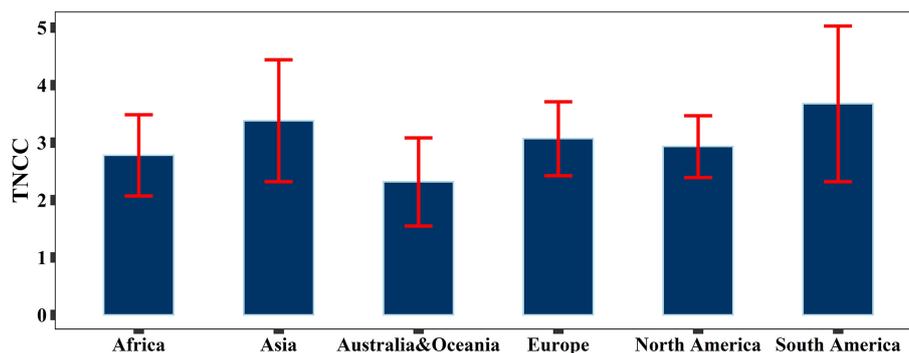

Figure 7. Statistics of GCI30-based TNCC during 2016 to 2018 at the continent level. The red line indicates the standard deviation (SD).

Province. The lowest CI occurred in the Australian Desert, with an average TNCC less than 2.

Overall, countries and AEZs with intensive farming are more subject to internal variability, as reflected by higher standard deviations (Fig. 8, right panel). Globally, there are 14 countries and 7 AEZs exhibiting standard deviations greater than 1.2, and most of them are located in South America and Asia. Regions with low CI averages but high CI

standard deviations were observed only on the western coast of South America and Queensland to Victoria in Australia, where partial irrigation in the former (Xie et al., 2019) and unstable rainfall in the latter resulted in diversified cropping intensities among years (King et al., 2020). The high standard deviations in Australia and Oceania mainly resulted from the high within-country and zonal heterogeneity, which may encompass aspects including the exceptionally variable climate
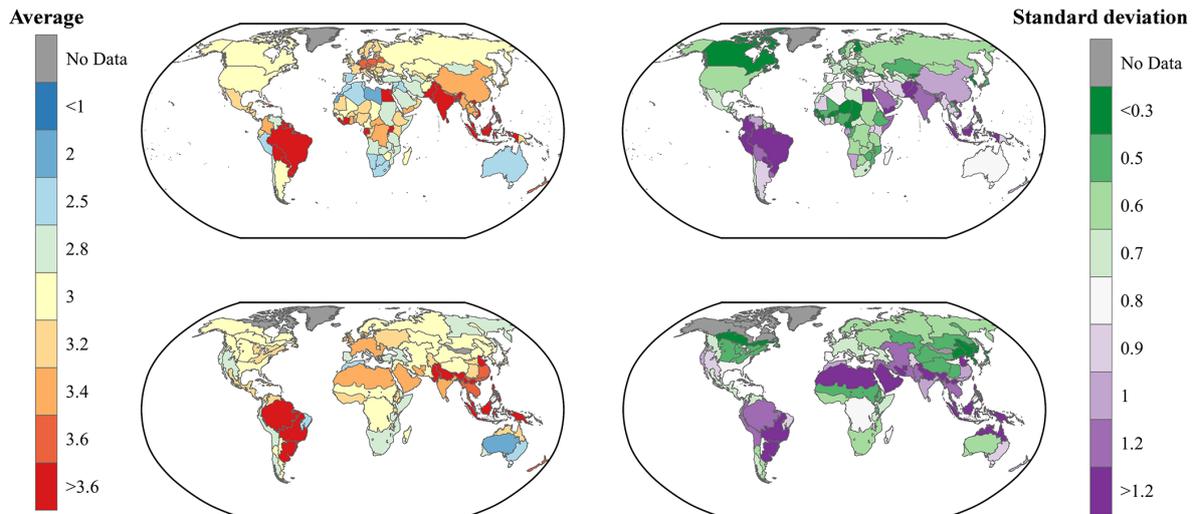
Figure 8. Average and standard deviation (SD) of TNCC during 2016 to 2018 at the national and AEZ levels.

with the prevalence of floods and droughts (King et al., 2020) and the annual shifting of crop types as well as cultivated and fallow lands (Song et al., 2017). In addition to these regular drivers, the political situation may cause CI spatiotemporal diversity. Notably, for instance, we found an unusually high standard deviation in Afghanistan, which was caused by both crop failure during the emergence to early development stages due to adverse weather conditions (Rousta et al., 2020) and abandoned cropland resulting from armed conflicts and refugee migrations (Iqbal et al., 2018; Galdo et al., 2020).

3.3 Cross-comparison with other studies

Due to the differences in methods, input data, and spatial resolution of the existing products containing CI metrics as listed in Table 2 and GCI30, the statistical average CI at global scales varied among the products. Based on GCI30, the global average CI during 2016–2018 was 1.05 (the continuous-cropping pixel excluded). Statistically, our CI is in a remarkably high agreement level with estimates based on the existing six estimates (mean CI: 1.09; median CI: 1.07), despite their significantly varying spatial resolution and temporal coverage. The minimum CI among the seven studies was estimated to be 0.84 per year based on the total cropland extent and the total harvested crop area reported by the agricultural statistics database of the United Nations Food and Agriculture Organization (FAO) FAO-STAT (FAOSTAT, 2019; Siebert et al., 2010). CI estimated by GCI30 is slightly higher than that derived from the FAO statistical database. The CI of other existing products listed in Table 2 ranges from 1.05, as estimated from the "NumCycles" layer of MCD12Q2 data (Gray et al., 2019), to 1.26, as evaluated by Wu et al. (2018). The statistics-based CI values estimated by Ray and Foley (2013) are lower than those estimated based on remote sensing data including the GCI30 and

those estimated by VIP4 and Wu et al. (2018) using AVHRR satellite observation data. The main reason is that statistics-based CI could not exclude the fallow land area as the agriculture statistics usually lack statistical information on fallow land, while fallow land could be identified using remote sensing (Zhang et al., 2014a, b) and excluded when generating satellite-based CI products. Our CI is also less than those CI products derived from AVHRR (VIP4 and Wu et al., 2018). On the one hand, the actual harvest frequency estimated by Wu et al. (2018) might overestimate the annual harvest areas and accordingly overestimate the cropping intensity because they may ignore the presence of fallowed cropland. Each pixel of cropland was assigned to either a single-cropping or double-cropping category, and fallow pixels were not considered, which will result in a higher CI (Wu et al., 2018). On the other hand, GCI30 systematically underestimates the cropping intensity when the harvest window is narrow between two growing seasons as a valid phenology season should include both green-up and green-down segments based on the GCI30 algorithm (C. Liu et al., 2020). Interestingly, our CI is exactly the same as the global average from MCD12Q2 for the years 2016 to 2018.

Figure 9 illustrated the differences in statistical annual CI at the country scale between GCI30 and four reference datasets. Statistical values of CI at the national scale are available in Table S4. National statistical CI values derived from GCI30 are in general close to that of MCD12Q2 and VIP4. The discrepancies of statistical CI values between GCI30 and those two products over a large proportion of countries range from −0.3 to 0.3. GCI30 and SACRA also present similar patterns of CI at the national scale, especially in Asia. GCI30 presents higher CI values in central Europe and Southeast Asia islands as well as Canada, Brazil, and Mexico. In contrast, positive difference values of cropping intensity were commonly observed all over the world as pre-
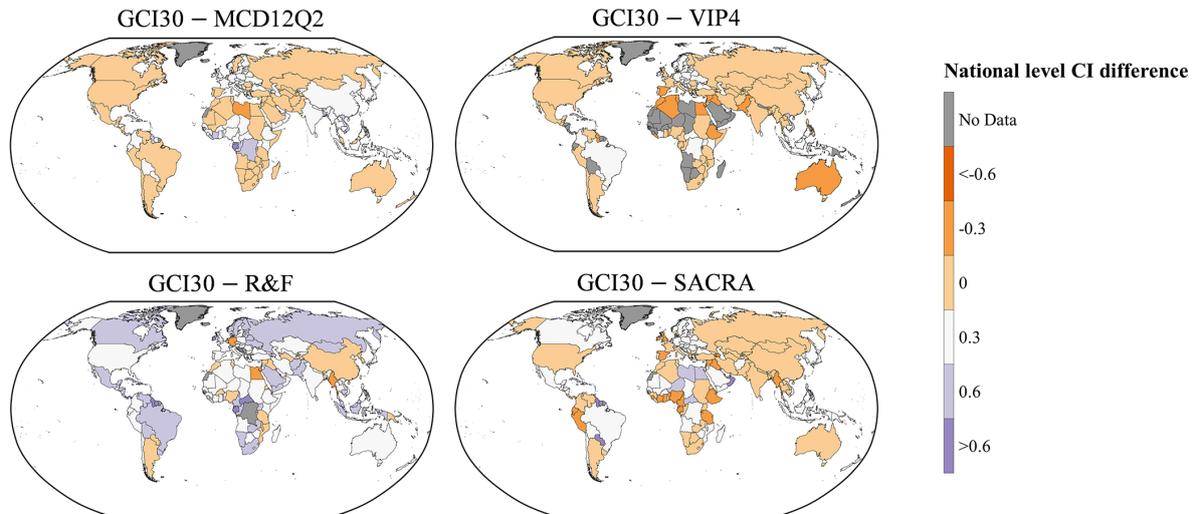
Figure 9. Statistics of annual CI differences at national level between GCI30 and four existing products. GCI30 − MCD12Q2 represents the differences between GCI30 and the "NumCycles" layer of MCD12Q2; GCI30 − VIP4 represents the differences between GCI30 and the "Number of Seasons" layer of VIP4; GCI30−R&F represents the differences between GCI30 and harvest frequency by Ray and Foley (2013); GCI30 − SACRA represents the differences between GCI30 and CI by Kotsuki and Tanaka (2015).

sented by the GCI30 – R&F map. Lower CI values are only observed in a few countries in Africa, Asia, and South America.

This study further compared the spatial pattern of the global CI difference between GCI30 and the two global land surface phenology products (MCD12Q2 and VIP4) at pixel level, as displayed in Fig. 10. Overall, all three products revealed consistent CI estimations across continents, with zero-difference pixels reaching 79 % or higher and the majority of CI differences ranging from −1 to 1. Spatially, positive CI difference values were commonly found in Southeast Asia, the Indian subcontinent, and some parts of Europe. Negative CI difference values, on the other hand, were mainly detected in North and South America. There were also discrepancies when these two phenology products were used as the baselines. Referring to MCD12Q2, there were many pixels showing positive values, especially in Africa and mainland China. However, the opposite tendency was observed using VIP4, which exhibited vast negative pixel distributions in Europe and the North China Plain.

To further explore how the CI difference varied over space, we selected four $15° \times 12°$ subregions (North America, South America, South Asia, and East Asia, which are labelled A, B, C, and D, respectively, in Fig. 10) that were representative of the global diversity of crop species, climate types, and management conditions. In general, substantial variations were detected through these spatially explicit maps. The strongest agreement between GCI30 and MCD12Q2 was found in East Asia (83 % of zero values), followed by North America and South Asia, with over 75 % agreement. The lowest agreement level occurred in South America, where 32 % of the GCI30 estimations showed pos-

itive or negative CI differences compared to the MCD12 output. Comparatively, the significant differences and corresponding spatial distributions between the GCI30 and VIP4 outputs had a low level of agreement, although the percentages of pixels with zero difference reached 50 % or higher for all subregions. Specifically, three out of the four subregions had at least one-fifth of the pixels featuring negative CI differences. The largest negative disagreement was detected in East Asia, where 41 % of the total cropland area had negative values, while North America and South America also had considerable negative proportions. Finally, in South Asia, the positive and negative pixel percentages were almost equal, i.e. half and half. Neither MCD12Q2 nor VIP4 should be considered to be ground truth. In fact, the reliability of these two land surface phenology products, especially VIP4, is affected by several factors, including a coarse spatial resolution, temporal mismatch, and algorithm structure differences when compared to GCI30. Taking East Asia as an example, the "cross-year season cycle" phenomenon (C. Liu et al., 2020) caused by winter wheat planting could lead to one more "partial growing season" being detected by VIP4 (Didan and Barreto, 2016), which largely explains why the CI difference between GCI30 and VIP4 shows an outstanding underestimation pattern.

3.4 Advantages and limitations of GCI30

As a global 30 m product, GCI30 depicts the worldwide diversity of agricultural land use intensity in a spatially explicit manner that has not been fully revealed by existing studies or datasets. Given the CI distribution with a fine spatial resolution, GCI30 is associated with reduced uncertainties
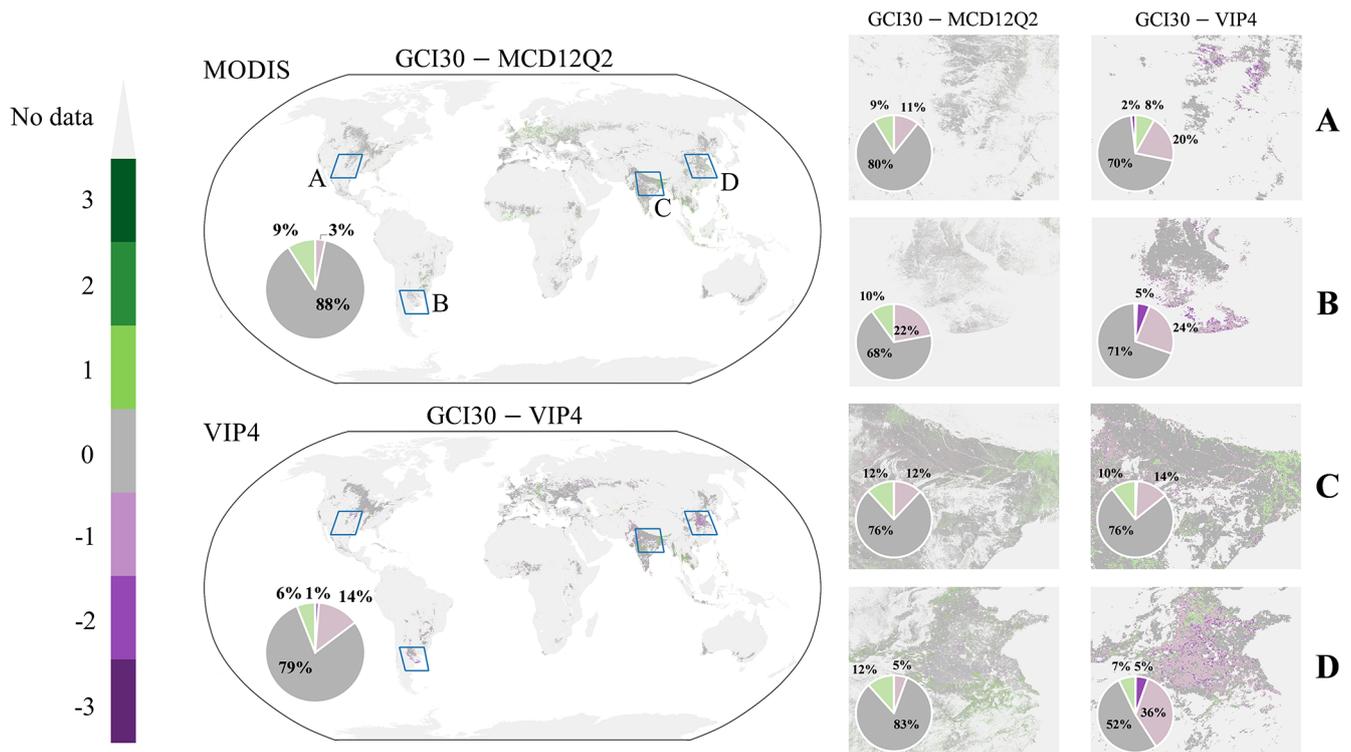
Figure 10. Spatial patterns and statistics of the CI differences among GCI30, MCD12Q2, and VIP4.

caused by the mixed-pixel effect. In addition to the improvement of mapping accuracy, GCI30 has the potential to monitor landscape-scale cropping practices on fragmented land parcels by smallholders, which comprise over half of the rural populations in developing nations that are most vulnerable to food security and environmental challenges (Morton et al., 2006; Jain et al., 2013; Lowder et al., 2016; C. Liu et al., 2020). Compared with the generalizable crop phenophase pattern, the GCI30 algorithm is not only efficient in mapping the CI distribution across various AEZs but is also flexible enough to be improved with updated data inputs. For example, the Harmonized Landsat and Sentinel-2 surface reflectance dataset (Claverie et al., 2018), with a 5 d revisit interval and a 30 m pixel size, is expected to enhance the global CI mapping performance once its worldwide coverage is ready. The successful production of GCI30 on the GEE platform illustrates a paradigm of mapping farming practices that is globally consistent and locally relevant using state-of-the-art cloud computing resources (Lewis et al., 2017; Amani et al., 2020; Tamiminia et al., 2020). It inspires future global fine-scale agricultural research that was previously not applicable.

A large number of natural factors and anthropogenic drivers are related to CI at the planetary scale. Accuracy assessments show that GCI30 explained over 91 % and 56 % of the sample variations examined by RDsat and RDsite, respectively (Fig. 3). The errors in GCI30 could be related to

the uncertainties in input data and limitations of the algorithm. The reliability of the cropland extent is a major factor constraining CI mapping performance. To minimize this effect, we integrated an ensemble of 10 land cover or specific cropland layer products for acquiring global cropland extent at a 30 m resolution for 2016–2018. Despite the high overall accuracy of the generated cropland extent, classification errors still exist, especially in some regions of Africa and Asia where small cropland patches are mixed with other land covers (Gong et al., 2013; Xiong et al., 2017). Although we follow the definition of cropland to select a subset of classes of a layer that best fit in the definition for each of the land-cover and cropland products, the inconsistency among the 10 land cover or specific cropland layer products still exists. The first issue is greenhouse farming, which is included in the cropland class in the FROM-GLC. However, the GCI30 product excluded the greenhouse pixels as CI of greenhouse crops is detected as zero cropping monitored by remote sensing. The second concern is the perennial woody crops such as orchards and vineyards from NLCD. As the NLCD data were only used for the Alaska region, they will have very limited impact on the integrated global cropland layer and accordingly a minor effect on GCI30. On the other hand, as no single product has yet been shown to be consistently accurate in representing cropland distribution, our approach by integrating a different dataset is still better than relying on

a single source of land cover or cropland layer (Fritz et al., 2015).

The GCI30 algorithm depends heavily on crop phenological information derived from the time series of vegetation indices. We found that the spatial pattern of the invalid observation count of the 16 d harmonized TOA reflectance composite (Fig. S2) matched well with those of the RDsat sample bias in some cloudy regions, such as the Gulf of Guinea and East African Highlands (Fig. 4), indicating that the performance of GCI30 may be limited in areas suffering from unfavourable weather conditions or extreme seasonal imbalances of clear observations. In particular, the presence of clouds in the early and mid agricultural growing season is preventing optical remote sensing satellites from accurate agricultural applications including cropping cycle detection (Whitcraft et al., 2015; Nabil et al., 2020). Thus, it is reasonable to use the proportion of the invalid number of 16 d composites during 2016–2018 as a quality indicator of the GCI30 product. Lower data qualities were observed in the Amazon, western Africa, South and Southeast Asia, and South and Southwest China than other regions due to the high cloudy frequency (Fig. S2). Although the cloud frequency is relatively low in western Russia and central Europe compared with the above cloud-prone regions (Whitcraft et al., 2015), the data quality is also low mainly due to the snow cover in winter and spring. We further evaluated the uncertainty in the GCI30 at the global scale. In general, the places with high uncertainty coincided with the cloud-prone regions, which might be a resultant of high invalid satellite observations (Fig. S2, S3). The fragmented agricultural fields and complex farming practices in the regions including western Africa, South and Southeast Asia, and the East African Highlands (Fritz et al., 2015) further broaden the uncertainty. In Argentina, the cropland field size is large, and the cloud presence is less frequent. However, large bias of cropping cycles and high uncertainties were commonly observed (Figs. 4, 5), which might be attributed to the omission of the poor crops stressed by the severe drought in the 2017–2018 agricultural year (Rivera et al., 2021). Rice paddies are fundamentally different from non-flooded croplands, which affects CI mapping performance. We designed a specific rice paddy CI identification approach by considering the influence of the "flooding and transplanting phase". While promising, its application was limited due to the lack of a specific rice paddy layer. Therefore, more improvements can be included, such as integrating synthetic-aperture radar (SAR) data time series for more accurate flood signal detection (Singha et al., 2019).

Additionally, it is noteworthy that the GCI30 product provides insight only into the current actual cropping intensity; however, it is not linked to the potential cropping cycles. To assess the CI gaps between potential and actual situations, climate models could be introduced to simulate the potential cropping cycles under long-term average weather conditions. The proposed method can be readily applied to other years to retrieve long-term CI maps, which will fill in the knowl-edge gaps of decades-long changes in cropping practices and interannual variations (Iizumi and Ramankutty, 2015). Such information is key to improving our understanding of the CI response to climate in a more granular manner.

4 Code and data availability

The GCI30 product is available on Harvard Dataverse: https://doi.org/10.7910/DVN/86M4PO (Zhang et al., 2020). It is the first 30 m resolution CI dataset covering a global extent. The GCI30 product was tiled into 504 files in GeoTIFF format with geographic projection. To be precise, the spatial resolution of the product is 0.00026949459°. Each GCI30 tile encompasses an area of $10° \times 10°$ and is named in the following format: "Cropping_Intensity_30m_2016_2018_$regions$.tif". The "regions" in the file name are determined as follows: N/S (Northern Hemisphere or Southern Hemisphere) followed by a two-digit latitude label of the tile's top-left corner and E/W (Eastern Hemisphere or Western Hemisphere) followed by a three-digit longitude label of the tile's top-left corner. Each GeoTIFF file includes two layers. The first layer is the average CI during the 3 years from 2016 to 2018, with the noData value or masked areas assigned as -1. The valid values for the first layer are 1, 2, and 3, representing single cropping, double cropping, or triple cropping, respectively. The second layer is the TNCC from 2016 to 2018 with a noData value or masked areas assigned to -1. The continuous-cropping type or the number of cropping cycles larger than three per year is assigned as 127 in the above-mentioned two layers. We also included a shapefile of the tiles named "CroppingIntensity_tiles_shapefile.rar" in the repository so that users could easily find their target tiles. The GCI30 product was generated on the GEE platform using JavaScript language developed by the authors. The GEE script as well as the auxiliary data of the GCI30 algorithm as an illustration for one tile is open to all potential users and available at https://code.earthengine.google.com/64f569c03f8fd633a896a3ec6f56b89a (Zhang and Liu, 2021). The code is openly available on the GEE platform, but users need a GEE account to access to it.

5 Conclusions

In this study, we utilized multisource remote sensing data, including Landsat, Sentinel-2, and MODIS data, to produce the first 30 m CI map at a global scale. Based on the phenophase-based mapping framework, GCI30 identified CI by enumerating the transition points between growing and non-growing periods. To improve the CI mapping performance on flooded rice paddies, we specifically considered the influence of the "flooding and transplanting signal" on the created phenophase profile. Accuracy assessments and intercomparisons with existing land surface phenology products

Earth Syst. Sci. Data, 13, 4799–4817, 2021

https://doi.org/10.5194/essd-13-4799-2021

suggested that GCI30 was reliable across different climate zones and cropping systems. According to GCI30, we estimated that the global average CI was 1.05 during 2016–2018. We found that single-cropping systems occupied more than 80 % of the world's cropland extent, while multiple-cropping practices were more commonly observed in South America and Asia than on other continents. National- and AEZ-level statistics demonstrated the joint influence of natural and anthropogenic drivers in controlling CI spatial patterns in most areas of the world. We concluded that the new GCI30 dataset provided improved estimates of global CI in a spatially explicit manner that has not been fully captured by previous studies or products and thus can serve to fill data gaps for promoting sustainable agriculture and achieving SDGs.

Author contributions. MZ and CL were responsible for the experimental design, data processing and analysing, paper preparation, revision, and presentation. BW contributed to the conceptual design, reviewing and revising the paper, funding acquisition, and project administration. GH provided support in experimental design, funding acquisition, and project administration. ST and QZ were responsible for data processing and analysing as well as reviewing and revising the paper. HZ, MN, FT, JB, ANB, AE, NY, ZW, and YL contributed to the validation data collection, performed data processing, and helped in paper revision.

Competing interests. The authors declare that they have no conflict of interest.

References

Amani, M., Ghorbanian, A., Ahmadi, S. A., Kakooei, M., Moghimi, A., Mirmazloumi, S. M., Moghaddam, S. H. A., Mahdavi, S., Ghahremanloo, M., and Parsian, S.: Google earth engine cloud computing platform for remote sensing big data applications: A comprehensive review, IEEE J. Sel. Top. Appl., 13, 5326–5350, https://doi.org/10.1109/JSTARS.2020.3021052, 2020.

Beck, H. E., Zimmermann, N. E., McVicar, T. R., Vergopolan, N., Berg, A., and Wood, E.: Present and future Köppen-Geiger climate classification maps at 1-km resolution, Scientific Data, 5, 180214, https://doi.org/10.1038/sdata.2018.214, 2018.

Becker, M. and Johnson, D. E.: Cropping intensity effects on upland rice yield and sustainability in West Africa, Nutr. Cycl. Agroecosys., 59, 107–117, https://doi.org/10.1023/A:1017551529813, 2001.

Bolton, D. K., Gray, J. M., Melaas, E. K., Moon, M., Eklundh, L., and Friedl, M. A.: Continental-scale land surface phenology from harmonized Landsat 8 and Sentinel-2 imagery, Remote Sens. Environ., 240, 111685, https://doi.org/10.1016/j.rse.2020.111685, 2020.

Challinor, A. J., Parkes, B., and Ramirez-Villegas, J.: Crop yield response to climate change varies with cropping intensity, Glob. Change Biol., 21, 1679–1688, https://doi.org/10.1111/gcb.12808, 2015.

Chastain, R., Housman, I., Goldstein, J., Finco, M., and Tenneson, K.: Empirical cross sensor comparison of Sentinel-2A and 2B MSI, Landsat-8 OLI, and Landsat-7 ETM+ top of atmosphere spectral characteristics over the conterminous United States, Remote Sens. Environ., 221, 274–285, https://doi.org/10.1016/j.rse.2018.11.012, 2019.

Chiew, F., Prosser, I., and Post, D.: On climate variability and climate change and impact on water resources, in: MODSIM 2011, 12–16 December 2011, Perth, Australia, Modelling and Simulation Society of Australia and New Zealand, 3553–3559, available at: http://hdl.handle.net/102.100.100/102035?index=1 (last access: 6 November 2020), 2011.

Claverie, M., Ju, J., Masek, J. G., Dungan, J. L., Vermote, E. F., Roger, J.-C., Skakun, S. V., and Justice, C.: The Harmonized Landsat and Sentinel-2 surface reflectance data set, Remote Sens. Environ., 219, 145–161, https://doi.org/10.1016/j.rse.2018.09.002, 2018.

Defourny, P., Bontemps, S., Bellemans, N., Cara, C., Dedieu, G., Guzzonato, E., Hagolle, O., Inglada, J., Nicola, L., and

Rabaute, T.: Near real-time agriculture monitoring at national scale at parcel resolution: Performance assessment of the Sen2-Agri automated system in various cropping systems around the world, Remote Sens. Environ., 221, 551–568, https://doi.org/10.1016/j.rse.2018.11.007, 2019.

Didan, K. and Barreto, A.: NASA MEaSUREs vegetation index and phenology (VIP) vegetation indices monthly global 0.05 Deg CMG, NASA EOSDIS Land Process, DAAC [data set], https://doi.org/10.5067/MEaSUREs/VIP/VIP15.004, 2016.

Ding, M., Chen, Q., Xiao, X., Xin, L., Zhang, G., and Li, L.: Variation in cropping intensity in northern China from 1982 to 2012 based on GIMMS-NDVI data, Sustainability, 8, 1123, https://doi.org/10.3390/su8111123, 2016.

Ding, M., Guan, Q., Li, L., Zhang, H., Liu, C., and Zhang, L.: Phenology-based rice paddy mapping using multi-source satellite imagery and a fusion algorithm applied to the Poyang Lake Plain, Southern China, Remote Sens., 12, 1022, https://doi.org/10.3390/rs12061022, 2020.

Dong, J. and Xiao, X.: Evolution of regional to global paddy rice mapping methods: A review, ISPRS J. Photogramm., 119, 214–227, https://doi.org/10.1016/j.isprsjprs.2016.05.010, 2016.

Dong, J., Xiao, X., Kou, W., Qin, Y., Zhang, G., Li, L., Jin, C., Zhou, Y., Wang, J., and Biradar, C.: Tracking the dynamics of paddy rice planting area in 1986–2010 through time series Landsat images and phenology-based algorithms, Remote Sens. Environ., 160, 99–113, https://doi.org/10.1016/j.rse.2015.01.004, 2015.

Dong, J., Xiao, X., Menarguez, M. A., Zhang, G., Qin, Y., Thau, D., Biradar, C., and Moore III, B.: Mapping paddy rice planting area in northeastern Asia with Landsat 8 images, phenology-based algorithm and Google Earth Engine, Remote Sens. Environ., 185, 142–154, https://doi.org/10.1016/j.rse.2016.02.016, 2016.

Eilers, P. H.: A perfect smoother, Anal. Chem., 75, 3631–3636, 2003.

Estel, S., Kuemmerle, T., Levers, C., Baumann, M., and Hostert, P.: Mapping cropland-use intensity across Europe using MODIS NDVI time series, Environ. Res. Lett., 11, 024015, https://doi.org/10.1088/1748-9326/11/2/024015, 2016.

FAO, IFAD, UNICEF, WFP, and WHO: The State of Food Security and Nutrition in the World 2020. Transforming food systems for affordable healthy diets, FAO, Rome, Italy, https://doi.org/10.4060/ca9692en, 2020.

FAOSTAT: FAOSTAT database, Food and Agriculture Organization of the United Nations (FAO), Rome, Italy [data set], available at: https://www.fao.org/faostat/en/#data, last access: 4 September 2019.

Fritz, S., McCallum, I., Schill, C., Perger, C., See, L., Schepaschenko, D., Van der Velde, M., Kraxner, F., and Obersteiner, M.: Geo-Wiki: An online platform for improving global land cover, Environ. Model Softw., 31, 110–123, https://doi.org/10.1016/j.envsoft.2011.11.015, 2012.

Fritz, S., See, L., McCallum, I., You, L., Bun, A., Moltchanova, E., Duerauer, M., Albrecht, F., Schill, C., Perger, C., Havlik, P., Mosnier, A., Thornton, P., Wood-Sichra, U., Herrero, M., Becker-Reshef, I., Justice, C., Hansen, M., Gong, P., Abdel Aziz, S., Cipriani, A., Cumani, R., Cecchi, G., Conchedda, G., Ferreira, S., Gomez, A., Haffani, M., Kayitakire, F., Malanding, J., Mueller, R., Newby, T., Nonguierma, A., Olusegun, A., Ortner, S., Rajak, D. R., Rocha, J., Schepaschenko, D., Schepaschenko, M., Terekhov, A., Tiangwa, A., Vancut-

sem, C., Vintrou, E., Wenbin, W., van der Velde, M., Dunwoody, A., Kraxner, F., and Obersteiner, M.: Mapping global cropland and field size, Glob. Change Biol., 21, 1980–1992, https://doi.org/10.1111/gcb.12838, 2015.

Galdo, V., Lopez-Acevedo, G., and Rama, M.: Conflict and the Composition of Economic Activity in Afghanistan, World Bank Policy Research Working Paper, The World Bank, Washington, D.C., USA, No. 9188, available at: https://ssrn.com/abstract= 3556240 (last access: 24 February 2021), 2020.

Gommes, R., Wu, B., Li, Z., and Zeng, H.: Design and characterization of spatial units for monitoring global impacts of environmental factors on major crops and food security, Food and Energy Security, 5, 40–55, https://doi.org/10.1002/fes3.73, 2016.

Gommes, R., Wu, B., Zhang, N., Feng, X., Zeng, H., Li, Z., and Chen, B.: CropWatch agroclimatic indicators (CWAIs) for weather impact assessment on global agriculture, Int. J. Biometeorol., 61, 199–215, https://doi.org/10.1007/s00484-016-1199-7, 2017.

Gong, P., Wang, J., Yu, L., Zhao, Y., Zhao, Y., Liang, L., Niu, Z., Huang, X., Fu, H., Liu, S., Li, C., Li, X., Fu, W., Liu, C., Xu, Y., Wang, X., Cheng, Q., Hu, L., Yao, W., Zhang, H., Zhu, P., Zhao, Z., Zhang, H., Zheng, Y., Ji, L., Zhang, Y., Chen, H., Yan, A., Guo, J., Yu, L., Wang, L., Liu, X., Shi, T., Zhu, M., Chen, Y., Yang, G., Tang, P., Xu, B., Giri, C., Clinton, N., Zhu, Z., Chen, J., and Chen, J.: Finer resolution observation and monitoring of global land cover: first mapping results with Landsat TM and ETM+ data, Int. J. Remote Sens., 34, 2607–2654, https://doi.org/10.1080/01431161.2012.748992, 2013.

Gorelick, N., Hancher, M., Dixon, M., Ilyushchenko, S., Thau, D., and Moore, R.: Google Earth Engine: Planetary-scale geospatial analysis for everyone, Remote Sens. Environ., 202, 18–27, https://doi.org/10.1016/j.rse.2017.06.031, 2017.

Gray, J., Friedl, M., Frolking, S., Ramankutty, N., Nelson, A., and Gumma, M. K.: Mapping Asian cropping intensity with MODIS, IEEE J. Sel. Top. Appl., 7, 3373–3379, https://doi.org/10.1109/JSTARS.2014.2344630, 2014.

Gray, J., Sulla-Menashe, D., and Friedl, M. A.: User guide to collection 6 modis land cover dynamics (mcd12q2) product, NASA EOSDIS Land Processes DAAC, Missoula, MT, USA, 2019.

Guo, H.: Big Earth data in support of the sustainable development goals (2019), Science Press and EDP Sciences, Beijing, China, 2021.

Guo, H., Bao, A., Liu, T., Ndayisaba, F., Jiang, L., Kurban, A., and De Maeyer, P.: Spatial and temporal characteristics of droughts in Central Asia during 1966–2015, Sci. Total Environ., 624, 1523–1538, https://doi.org/10.1016/j.scitotenv.2017.12.120, 2018.

Hao, L., Sun, G., Liu, Y., Wan, J., Qin, M., Qian, H., Liu, C., Zheng, J., John, R., Fan, P., and Chen, J.: Urbanization dramatically altered the water balances of a paddy field-dominated basin in southern China, Hydrol. Earth Syst. Sci., 19, 3319–3331, https://doi.org/10.5194/hess-19-3319-2015, 2015.

Hao, P.-Y., Tang, H.-J., Chen, Z.-X., Le, Y. U., and Wu, M.-Q.: High resolution crop intensity mapping using harmonized Landsat-8 and Sentinel-2 data, J. Integr. Agr., 18, 2883–2897, https://doi.org/10.1016/S2095-3119(19)62599-2, 2019.

Hinz, R., Sulser, T. B., Hüfner, R., Mason-D'Croz, D., Dunston, S., Nautiyal, S., Ringler, C., Schüngel, J., Tikhile, P., and Wimmer, F.: Agricultural development and land use change in India: A scenario analysis of trade-offs between UN Sustainable

Development Goals (SDGs), Earth's Future, 8, e2019EF001287, https://doi.org/10.1029/2019EF001287, 2020.

Iizumi, T. and Ramankutty, N.: How do weather and climate influence cropping area and intensity?, Global Food Security, 4, 46–50, https://doi.org/10.1016/j.gfs.2014.11.003, 2015.

Iqbal, M. W., Donjadee, S., Kwanyuen, B., and Liu, S.-y.: Farmers' perceptions of and adaptations to drought in Herat Province, Afghanistan, J. Mt. Sci., 15, 1741–1756, https://doi.org/10.1007/s11629-017-4750-z, 2018.

Jain, M., Mondal, P., DeFries, R. S., Small, C., and Galford, G. L.: Mapping cropping intensity of smallholder farms: A comparison of methods using multiple sensors, Remote Sens. Environ., 134, 210–223, https://doi.org/10.1016/j.rse.2013.02.029, 2013.

Jankowski, K., Neill, C., Davidson, E. A., Macedo, M. N., Costa, C., Galford, G. L., Santos, L. M., Lefebvre, P., Nunes, D., and Cerri, C. E. P.: Deep soils modify environmental consequences of increased nitrogen fertilizer use in intensifying Amazon agriculture, Sci. Rep., 8, 13478, https://doi.org/10.1038/s41598-018-31175-1, 2018.

King, A. D., Pitman, A. J., Henley, B. J., Ukkola, A. M., and Brown, J. R.: The role of climate variability in Australian drought, Nat. Clim. Change, 10, 177–179, https://doi.org/10.1038/s41558-020-0718-z, 2020.

Kong, D., Zhang, Y., Gu, X., and Wang, D.: A robust method for reconstructing global MODIS EVI time series on the Google Earth Engine, ISPRS J. Photogramm., 155, 13–24, https://doi.org/10.1016/j.isprsjprs.2019.06.014, 2019.

Kontgis, C., Schneider, A., and Ozdogan, M.: Mapping rice paddy extent and intensification in the Vietnamese Mekong River Delta with dense time stacks of Landsat data, Remote Sens. Environ., 169, 255–269, https://doi.org/10.1016/j.rse.2015.08.004, 2015.

Köppen, W., Volken, E., and Brönnimann, S.: The thermal zones of the earth according to the duration of hot, moderate and cold periods and to the impact of heat on the organic world, Meteorol. Z., 20, 351–360, https://doi.org/10.1127/0941-2948/2011/105, 2011.

Kotsuki, S. and Tanaka, K.: SACRA – a method for the estimation of global high-resolution crop calendars from a satellite-sensed NDVI, Hydrol. Earth Syst. Sci., 19, 4441–4461, https://doi.org/10.5194/hess-19-4441-2015, 2015.

Lal, R.: Soil carbon dynamics in cropland and rangeland, Environ. Poll., 116, 353–362, https://doi.org/10.1016/S0269-7491(01)00211-1, 2002.

Lewis, A., Oliver, S., Lymburner, L., Evans, B., Wyborn, L., Mueller, N., Raevksi, G., Hooke, J., Woodcock, R., and Sixsmith, J.: The Australian geoscience data cube – foundations and lessons learned, Remote Sens. Environ., 202, 276–292, https://doi.org/10.1016/j.rse.2017.03.015, 2017.

Li, L., Friedl, M. A., Xin, Q., Gray, J., Pan, Y., and Frolking, S.: Mapping crop cycles in China using MODIS-EVI time series, Remote Sens., 6, 2473–2493, https://doi.org/10.3390/rs6032473, 2014.

Liu, C., Zhang, Q., Tao, S., Qi, J., Ding, M., Guan, Q., Wu, B., Zhang, M., Nabil, M., and Tian, F.: A new framework to map fine resolution cropping intensity across the globe: Algorithm, validation, and implication, Remote Sens. Environ., 251, 112095, https://doi.org/10.1016/j.rse.2020.112095, 2020.

Liu, H., Gong, P., Wang, J., Clinton, N., Bai, Y., and Liang, S.: Annual dynamics of global land cover and its long-term changes from 1982 to 2015, Earth Syst. Sci. Data, 12, 1217–1243, https://doi.org/10.5194/essd-12-1217-2020, 2020.

Liu, L., Xiao, X., Qin, Y., Wang, J., Xu, X., Hu, Y., and Qiao, Z.: Mapping cropping intensity in China using time series Landsat and Sentinel-2 images and Google Earth Engine, Remote Sens. Environ., 239, 111624, https://doi.org/10.1016/j.rse.2019.111624, 2020.

Lowder, S. K., Skoet, J., and Raney, T.: The number, size, and distribution of farms, smallholder farms, and family farms worldwide, World Dev., 87, 16–29, https://doi.org/10.1016/j.worlddev.2015.10.041, 2016.

Mason-D'Croz, D., Sulser, T. B., Wiebe, K., Rosegrant, M. W., Lowder, S. K., Nin-Pratt, A., Willenbockel, D., Robinson, S., Zhu, T., and Cenacchi, N.: Agricultural investments and hunger in Africa modeling potential contributions to SDG2–Zero Hunger, World Dev., 116, 38–53, https://doi.org/10.1016/j.worlddev.2018.12.006, 2019.

Morton, D. C., DeFries, R. S., Shimabukuro, Y. E., Anderson, L. O., Arai, E., del Bon Espirito-Santo, F., Freitas, R., and Morisette, J.: Cropland expansion changes deforestation dynamics in the southern Brazilian Amazon, P. Natl. Acad. Sci. USA, 103, 14637–14641, https://doi.org/10.1073/pnas.0606377103, 2006.

Nabil, M., Zhang, M., Bofana, J., Wu, B., Stein, A., Dong, T., Zeng, H., and Shang, J.: Assessing factors impacting the spatial discrepancy of remote sensing based cropland products: A case study in Africa, Int. J. Appl. Earth Obs., 85, 102010, https://doi.org/10.1016/j.jag.2019.102010, 2020.

Oliver, M. A. and Webster, R.: Kriging: a method of interpolation for geographical information systems, Int. J. Geogr. Inf. Syst., 4, 313–332, https://doi.org/10.1080/02693799008941549, 1990.

Pielke Sr., R. A., Adegoke, J. O., Chase, T. N., Marshall, C. H., Matsui, T., and Niyogi, D.: A new paradigm for assessing the role of agriculture in the climate system and in climate change, Agr. Forest Meteorol., 142, 234–254, https://doi.org/10.1016/j.agrformet.2006.06.012, 2007.

Qiu, S., Zhu, Z., and He, B.: Fmask 4.0: Improved cloud and cloud shadow detection in Landsats 4–8 and Sentinel-2 imagery, Remote Sens. Environ., 231, 111205, https://doi.org/10.1016/j.rse.2019.05.024, 2019.

Ray, D. K. and Foley, J. A.: Increasing global crop harvest frequency: recent trends and future directions, Environ. Res. Lett., 8, 044041, https://doi.org/10.1088/1748-9326/8/4/044041, 2013.

Richardson, A. D., Hufkens, K., Milliman, T., and Frolking, S.: Intercomparison of phenological transition dates derived from the PhenoCam Dataset V1. 0 and MODIS satellite remote sensing, Sci. Rep., 8, 5679, https://doi.org/10.1038/s41598-018-23804-6, 2018a.

Richardson, A. D., Hufkens, K., Milliman, T., Aubrecht, D. M., Chen, M., Gray, J. M., Johnston, M. R., Keenan, T. F., Klosterman, S. T., and Kosmala, M.: Tracking vegetation phenology across diverse North American biomes using PhenoCam imagery, Scientific Data, 5, 180028, https://doi.org/10.1038/sdata.2018.28, 2018b.

Rivera, J. A., Otta, S., Lauro, C., and Zazulie, N.: A decade of hydrological drought in Central-Western Argentina, Frontiers in Water, 3, 640544, https://doi.org/10.3389/frwa.2021.640544, 2021.

Rousta, I., Olafsson, H., Moniruzzaman, M., Zhang, H., Liou, Y.-A., Mushore, T. D., and Gupta, A.: Impacts of drought

on vegetation assessed by vegetation indices and meteorological factors in Afghanistan, Remote Sens., 12, 2433, https://doi.org/10.3390/rs12152433, 2020.

Seyednasrollah, B., Young, A. M., Hufkens, K., Milliman, T., Friedl, M. A., Frolking, S., and Richardson, A. D.: Tracking vegetation phenology across diverse biomes using Version 2.0 of the PhenoCam Dataset, Scientific Data, 6, 222, https://doi.org/10.1038/s41597-019-0229-9, 2019.

Sherrod, L. A., Peterson, G. A., Westfall, D. G., and Ahuja, L. R.: Cropping intensity enhances soil organic carbon and nitrogen in a no-till agroecosystem, Soil Sci. Soc. Am. J., 67, 1533–1543, https://doi.org/10.2136/sssaj2003.1533, 2003.

Siebert, S., Portmann, F. T., and Döll, P.: Global patterns of cropland use intensity, Remote Sens., 2, 1625–1643, https://doi.org/10.3390/rs2071625, 2010.

Singha, M., Dong, J., Zhang, G., and Xiao, X.: High resolution paddy rice maps in cloud-prone Bangladesh and Northeast India using Sentinel-1 data, Scientific Data, 6, 26, https://doi.org/10.1038/s41597-019-0036-3, 2019.

Song, X.-P., Potapov, P. V., Krylov, A., King, L., Di Bella, C. M., Hudson, A., Khan, A., Adusei, B., Stehman, S. V., and Hansen, M. C.: National-scale soybean mapping and area estimation in the United States using medium resolution satellite imagery and field survey, Remote Sens. Environ., 190, 383–395, https://doi.org/10.1016/j.rse.2017.01.008, 2017.

Tamiminia, H., Salehi, B., Mahdianpari, M., Quackenbush, L., Adeli, S., and Brisco, B.: Google Earth Engine for geo-big data applications: A meta-analysis and systematic review, ISPRS J. Photogramm., 164, 152–170, https://doi.org/10.1016/j.isprsjprs.2020.04.001, 2020.

Tilman, D., Balzer, C., Hill, J., and Befort, B. L.: Global food demand and the sustainable intensification of agriculture, P. Natl. Acad. Sci. USA, 108, 20260–20264, https://doi.org/10.1073/pnas.1116437108, 2011.

UN: Transforming our world: the 2030 Agenda for Sustainable Development, UN General Assembly, United Nations, New York, NY, USA, 2015.

Waha, K., Dietrich, J. P., Portmann, F. T., Siebert, S., Thornton, P. K., Bondeau, A., and Herrero, M.: Multiple cropping systems of the world and the potential for increasing cropping intensity, Global Environ. Change, 64, 102131, https://doi.org/10.1016/j.gloenvcha.2020.102131, 2020.

Waldner, F., De Abelleyra, D., Verón, S. R., Zhang, M., Wu, B., Plotnikov, D., Bartalev, S., Lavreniuk, M., Skakun, S., and Kussul, N.: Towards a set of agrosystem-specific cropland mapping methods to address the global cropland diversity, Int. J. Remote Sens., 37, 3196–3231, https://doi.org/10.1080/01431161.2016.1194545, 2016.

Whitcraft, A. K., Vermote, E. F., Becker-Reshef, I., and Justice, C. O.: Cloud cover throughout the agricultural growing season: Impacts on passive optical earth observations, Remote Sens. Environ., 156, 438–447, https://doi.org/10.1016/j.rse.2014.10.009, 2015.

Whitcraft, A. K., Becker-Reshef, I., Justice, C. O., Gifford, L., Kavvada, A., and Jarvis, I.: No pixel left behind: Toward integrating Earth Observations for agriculture into the United Nations Sustainable Development Goals framework, Remote Sens. Environ., 235, 111470, https://doi.org/10.1016/j.rse.2019.111470, 2019.

Wu, B., Ahmed, S., and He, C.: Shared Agronomic Information Community for the Belt and Road Initiative, Bulletin of Chinese Academy of Sciences, 32, 34–41, 2017.

Wu, W., Yu, Q., You, L., Chen, K., Tang, H., and Liu, J.: Global cropping intensity gaps: Increasing food production without cropland expansion, Land Use Policy, 76, 515–525, https://doi.org/10.1016/j.landusepol.2018.02.032, 2018.

Xiao, X., Boles, S., Liu, J., Zhuang, D., Frolking, S., Li, C., Salas, W., and Moore Iii, B.: Mapping paddy rice agriculture in southern China using multi-temporal MODIS images, Remote Sens. Environ., 95, 480–492, https://doi.org/10.1016/j.rse.2004.12.009, 2005.

Xie, Y., Lark, T. J., Brown, J. F., and Gibbs, H. K.: Mapping irrigated cropland extent across the conterminous United States at 30 m resolution using a semi-automatic training approach on Google Earth Engine, ISPRS J. Photogramm., 155, 136–149, https://doi.org/10.1016/j.isprsjprs.2019.07.005, 2019.

Xiong, J., Thenkabail, P. S., Tilton, J. C., Gumma, M. K., Teluguntla, P., Oliphant, A., Congalton, R. G., Yadav, K., and Gorelick, N.: Nominal 30 m cropland extent map of continental Africa by integrating pixel-based and object-based algorithms using Sentinel-2 and Landsat-8 data on Google Earth Engine, Remote Sens., 9, 1065, https://doi.org/10.3390/rs9101065, 2017.

Yan, H., Xiao, X., Huang, H., Liu, J., Chen, J., and Bai, X.: Multiple cropping intensity in China derived from agro-meteorological observations and MODIS data, Chinese Geogr. Sci., 24, 205–219, https://doi.org/10.1007/s11769-013-0637-2, 2014.

Yan, H., Liu, F., Qin, Y., Doughty, R., and Xiao, X.: Tracking the spatio-temporal change of cropping intensity in China during 2000–2015, Environ. Res. Lett., 14, 035008, https://doi.org/10.1088/1748-9326/aaf9c7, 2019.

Zeng, Z., Estes, L., Ziegler, A. D., Chen, A., Searchinger, T., Hua, F., Guan, K., Jintrawet, A., and Wood, E. F.: Highland cropland expansion and forest loss in Southeast Asia in the twenty-first century, Nat. Geosci., 11, 556–562, https://doi.org/10.1038/s41561-018-0166-9, 2018.

Zhang, M. and Liu, C.: The script of core GCI30 algorithm on Google Earth Engine, Google Earth Engine (GEE) [code], available at: https://code.earthengine.google.com/64f569c03f8fd633a896a3ec6f56b89a, last access: 29 September 2021.

Zhang, M., Wu, B., Meng, J., Dong, T., and You, X.: Fallow land mapping for better crop monitoring in Huang-Huai-Hai Plain using HJ-1 CCD data, IOP Conf. Ser.: Earth Environ. Sci., 17, 012048, https://doi.org/10.1088/1755-1315/17/1/012048, 2014a.

Zhang, M., Wu, B., Yu, M., Zou, W., and Zheng, Y.: Crop condition assessment with adjusted NDVI using the uncropped arable land ratio, Remote Sens., 6, 5774–5794, https://doi.org/10.3390/rs6065774, 2014b.

Zhang, M., Wu, B., Zeng, H., He, G., Liu, C., Nabil, M., Tian, F., Bofana, J., Wang, Z., and Yan, N.: GCI30: Global Cropping Intensity at 30 m resolution (2), V2, Harvard Dataverse [data set], https://doi.org/10.7910/DVN/86M4PO, 2020.

Zhang, Y., Kong, D., Gan, R., Chiew, F. H., McVicar, T. R., Zhang, Q., and Yang, Y.: Coupled estimation of 500 m and 8-day resolution global evapotranspiration and gross primary production in 2002–2017, Remote Sens. Environ., 222, 165–182, https://doi.org/10.1016/j.rse.2018.12.031, 2019.

Zhu, Z. and Woodcock, C. E.: Object-based cloud and cloud shadow detection in Landsat imagery, Remote Sens. Environ., 118, 83–94, https://doi.org/10.1016/j.rse.2011.10.028, 2012.

Zohaib, M. and Choi, M.: Satellite-based global-scale irrigation water use and its contemporary trends, Sci. Total Environ., 714, 136719, https://doi.org/10.1016/j.scitotenv.2020.136719, 2020.

https://doi.org/10.5194/essd-13-4799-2021

Earth Syst. Sci. Data, 13, 4799–4817, 2021